AGU100 ADVANCING EARTH AND SPACE SCIENCE

Water Resources Research

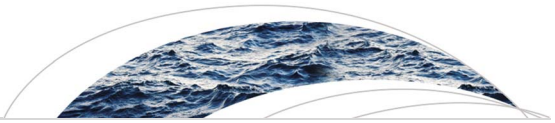

RESEARCH ARTICLE
10.1029/2018WR023032

Key Points:
- Microbially induced $CaCO_3$ precipitation (MICP) was successfully applied to seal microsized fractures in granite cores
- Microscale analyses show $CaCO_3$ strongly attached to both fracture surfaces, in places completely bridging the aperture
- MICP grouted fractures have the potential to provide additional mechanical stability to the rock mass as well as provide a hydraulic barrier

Supporting Information:
- Supporting Information S1

Correspondence to:
D. J. Tobler,
dominique.tobler@nano.ku.dk

Citation:
Tobler, D. J., Minto, J. M., El Mountassir, G., Lunn, R. J., & Phoenix, V. R. (2018). Microscale analysis of fractured rock sealed with microbially induced $CaCO_3$ precipitation: Influence on hydraulic and mechanical performance. *Water Resources Research*, *54*. https://doi.org/10.1029/2018WR023032

Received 28 MAR 2018
Accepted 10 SEP 2018
Accepted article online 24 SEP 2018

Microscale Analysis of Fractured Rock Sealed With Microbially Induced $CaCO_3$ Precipitation: Influence on Hydraulic and Mechanical Performance

Dominique J. Tobler[1,2], James M. Minto[3], Gráinne El Mountassir[3], Rebecca J. Lunn[3], and Vernon R. Phoenix[2,3]

[1]Nano-Science Center, Department of Chemistry, University of Copenhagen, Copenhagen, Denmark, [2]School of Geographical and Earth Sciences, University of Glasgow, Glasgow, UK, [3]Department of Civil and Environmental Engineering, University of Strathclyde, Glasgow, UK

Abstract Microbially induced $CaCO_3$ precipitation (MICP) has shown great potential to reduce permeability in intact rocks as a means to seal fluid pathways in subsurface ground, for example, to secure waste storage repositories. However, much less is known about how to apply MICP to seal fractured rock. Furthermore, there is limited information on the hydraulic and mechanical properties of MICP filled fractures, which are essential criteria to assess seal performance. Here MICP injection strategies were tested on sandstone cores, aimed at obtaining a homogeneous porosity fill that reduced permeability by 3 orders of magnitude. The injection strategy resulting in the most homogenous calcite distribution was then applied to fractured granite cores, to yield transmissivity reduction of up to 4 orders of magnitude. Microscale analysis of these sealed granite cores using X-ray-computed tomography and electron microscopy showed that >67% of the fracture aperture was filled with calcite, with crystals growing from both fracture planes, and bridging the fracture aperture in several places. Shear strength tests performed on these cores showed that the peak shear strength correlated well with the percentage of the fracture area where calcite bridged the aperture. Notably, brittle failure occurred within the MICP grout, showing that the calcite crystals were strongly attached to the granite surface. If MICP fracture-sealing strategies can be designed such that the majority of $CaCO_3$ crystals bridge across the fracture aperture, then MICP has the potential to provide significant mechanical stability to the rock mass as well as forming a hydraulic barrier.

1. Introduction

There is significant interest in using microbially induced $CaCO_3$ precipitation (MICP) to reduce the permeability of porous and fractured media (e.g., Cunningham et al., 2014; Cuthbert et al., 2013; Minto et al., 2016, 2017; Phillips et al., 2016; Tobler et al., 2012). As such MICP has been proposed for use in the creation of subsurface barriers in a range of different contexts including fracture grouting in deep geological disposal of nuclear waste, to reduce leakage from carbon sequestration reservoirs and to enhance recovery from oil and gas reservoirs (Cunningham et al., 2014; Cuthbert et al., 2013; Ferris & Stehmeier, 1992; Minto et al., 2017; Mitchell et al., 2013; Phillips et al., 2013, 2016). Considering the context of deep geological disposal of nuclear waste, MICP is particularly suitable for sealing fine aperture fractures (<100 μm) due to its low viscosity and small size of the bacteria (a few microns), enabling excellent penetration. In contrast cement grouts are characterized by their larger particle size, high initial viscosities (which increase over time), and their requirement for high injection pressures to initiate flow. Furthermore, MICP reagents have a low pH (<11) unlike cement; this is required as highly alkaline plumes can negatively impact on the performance of bentonite buffers surrounding the nuclear waste cannisters (Bodén and Sievänen, 2005). Moreover, cements undergo volumetric shrinkage during setting, creating microcracks, and their permeability seems to further increase with aging (Laver et al., 2013).

The long-term performance of the hydraulic barrier created by MICP is a key consideration for its deployment in nuclear waste repositories. To date the chemical durability of MICP barriers has been investigated by Minto et al. (2017), who demonstrated that seal performance can be maintained even in acidic conditions. However, little remains known about the mechanical durability of MICP in fractured rock. If mechanical failure of the MICP seal were to occur, for example, due to stress redistributions, then hydraulic flow could be reinitiated. In a nuclear waste disposal context, this has two possible consequences: (i) the previously sealed fractures

could act as migration pathways for radionuclides, but also (ii) if glacial meltwater intrusion occurs (up to eight glaciation periods may be expected within a repository timescale), it can result in the erosion of the bentonite buffer (Reid et al., 2015), which is one of the main barriers limiting migration of radionuclides to the biosphere. The shearing response of MICP grouted fractures has not previously been investigated.

A variety of MICP processes exist, controlled by different metabolic pathways, for example, photosynthesis, denitrification, sulphate reduction, ammonification, and methane oxidation (Zhu & Dittrich, 2016, and references therein). The process that has shown the greatest promise, however, is ureolysis-driven $CaCO_3$ precipitation. In this process, ureolytic bacteria hydrolyse urea, producing ammonium and carbonate as by-products. This leads to a pH increase, which in the presence of dissolved calcium, induces the precipitation of $CaCO_3$ minerals. Calcite is the most thermodynamically stable $CaCO_3$ phase and is often observed as the main mineral in this process (Tobler et al., 2011, 2012). Vaterite often forms as an intermediate phase prior to calcite; however, it is less frequently observed in MICP studies because it is unstable in solution and transforms to calcite within hours/days depending on conditions (Rodriguez-Blanco et al., 2017). Aragonite, another $CaCO_3$ polymorph is only stable at higher temperatures and/or in the presence of specific ions such as Mg (Rodriguez-Blanco et al., 2012).

The ureolytic strain most commonly used in MICP studies is *Sporocarsina pasteurii*, a halotolerant, soil bacterium, which has shown high ureolytic activity under both anaerobic and aerobic conditions (Tobler et al., 2011), within porous media (Dejong et al., 2013; Van Paassen et al., 2010; Phillips et al., 2013; Sham et al., 2013; Tobler et al., 2012; Whiffin et al., 2007), and at different salinities, temperatures, and pressures (Ferris et al., 2003; Mitchell & Ferris, 2005; Mitchell et al., 2010, 2013; Verba et al., 2016). While *S. pasteurii* can perform well under a wide range of subsurface conditions, the challenge often faced when implementing this technique in subsurface rock (Cunningham et al., 2014; Cuthbert et al., 2013; Phillips et al., 2016), is the lack of control on the distribution of the forming precipitate, leading to heterogeneous porosity reduction and a rapid decrease in permeability local to the injection point (i.e., clogging). This can be explained by several factors. MICP has to date been most widely studied in sand columns, where different injection strategies are applied and permeability reduction is determined, with little information given on the spatial distribution of the calcite fill. Moreover, sand columns are designed to be homogeneous, thus these experiments lack the complexity of natural systems (i.e., heterogeneities in hydrodynamics, geometry, geochemistry, and mineralogy), which all influence how microbes move through pores and fractures, as well as how active they are once immobilized. This was demonstrated in previous work (Tobler et al., 2014), where *S. pasteurii* transport in sandstone was quantified as a function of different core lengths, bacterial densities, and flow rates. Even in rock with a high degree of homogeneity, *S. pasteurii* will have considerably different transport characteristics than in packed sand and this cannot be described with current models (Tobler et al., 2014).

The few laboratory studies performed on MICP in rock matrices (Cunningham et al., 2014; Minto et al., 2017; Phillips et al., 2013; Sham et al., 2013) have shown that MICP can be used to greatly reduce the permeability of both porous and fractured rocks when the system is pressurized (in some systems up to 7.6 MPa). However, little is known about the distribution of the bacterial cells in these systems and how this then impacts on the extent and distribution of the calcite precipitate. El Mountassir et al. (2014) and Minto et al. (2016) visualized MICP precipitation in rock fractures via a transparent polycarbonate upper fracture surface. These studies demonstrated the influence of fluid velocity on controlling bacterial transport in fractures and the subsequent distribution of calcite. However, the polycarbonate fracture surfaces typically showed lower calcite precipitation than the rock surfaces. The successful field studies performed in subsurface rock fractures to date (Cunningham et al., 2014; Cuthbert et al., 2013; Phillips et al., 2016) have clearly demonstrated that the use of MICP for groundwater control in subsurface rock is getting close to commercialization while also providing key data on encountered subsurface hydrogeochemical conditions and how these control the injection strategies that can be employed. At the same time, however, there is still much to learn on the micrometer scale interactions between microbes, minerals and the fluids that occur in pore spaces and throats and within fractures, impacting bacterial transport through rocks and ultimately, the extent and distribution of calcite formation within the rock matrix. Moreover, in order to optimize injection strategies for field scale investigation and eventual commercialization of this technology, it is paramount to assess the hydraulic and mechanical performance of MICP filled fractures and to determine how they are controlled by the spatial distribution of the calcite fill.

The objectives of this study were therefore to

1. perform initial MICP grouting tests in porous sandstone to determine the injection strategy which resulted in the most homogeneous calcite precipitation;
2. apply the most successful injection strategy to grout fractures in granite cores and determine the effectiveness of MICP at reducing fracture aperture and transmissivity.
3. examine the texture and distribution of the $CaCO_3$ precipitate within the grouted granite fracture and evaluate potential links to the applied injection approach and rock fracture properties; and
4. quantify the shear strength of the grouted granite fracture and compare with the observed spatial characteristics of the $CaCO_3$ precipitate to evaluate the potential use of MICP for rock fracture grouting.

2. Materials and Methods

2.1. Experimental Setup

In order to determine an injection strategy for achieving homogeneous $CaCO_3$ precipitation in rocks, three Bentheimer sandstone rock cores (75-mm length, 37-mm diameter; Kocurek Industries) were treated with MICP using the same high-pressure system but different injection strategies (section 2.2). The system consisted of two high-pressure isocratic pumps and a Hassler core holder (TEMCO Inc., Tulsa, OK). The core holder was connected to a backpressure regulator via a double valve to obtain a confining pressure of 1.7 MPa on the core. The increase in backpressure due to plugging was monitored using a pressure gauge connected to the inlet of the core holder. Prior to loading, the sandstone cores were saturated with deionized water (under vacuum). The initial porosity of the sandstone cores was 23% as determined gravimetrically. The permeability, k (cm^2), was calculated from the pressure difference across the core (equal to the backpressure), ΔP, using the following equation:

$$k = \frac{QL\mu}{A\Delta P}$$

where Q is the flow rate, A the core cross-sectional area, L the core length, and μ the dynamic viscosity. The initial permeability of the untreated sandstone was determined in the low-pressure flow through setup (see below) by measuring the hydraulic head at three different flow rates, yielding an average k value of 2.4×10^{-8} cm^2.

Four granite cores (36 mm length, 36 mm diameter) were fractured artificially by sawing the core in half along its length. Crushed granite grains were used as spacers (along the side of the core) to create a fracture with an aperture of approximately 300 μm and a volume of 0.39 cm^3 and then wrapped in parafilm to hold the core together. Plugging of the fractured granite cores was started in low-pressure flow-through cells so all four cores could be treated at the same time, with the same bacterial suspensions. For this, the cores were placed inside silicon tubing (36-mm diameter) permitting a tight fit and then amended with Teflon inlet and outlet ports. Solutions were pumped through the fractured granite cores (with the fracture plane positioned horizontally) using a peristaltic pump. Once a backpressure of approximately 7 kPa was reached, the granite cores were transferred to the Hassler Core holder setup (described above) to permit a higher degree of cementation and higher backpressures. The fracture transmissivity, T (m^2/s), was calculated using the following equation based on the parallel plate cubic law for laminar flow in fractures (Witherspoon et al., 1980):

$$T = \frac{QL}{\Delta hW}$$

where Q is the flow rate, L and W the fracture length and width, respectively, and Δh the head loss between the fracture inlet and outlet (calculated from the measured backpressure). The initial transmissivity of the untreated fractured granite cores was determined in the low-pressure flow through setup by measuring the hydraulic head at three different flow rates, yielding an average value of 7.1×10^{-7} m^2/s.

2.2. Injection Approach

A suspension of the urease positive strain *Sporosarcina pasteurii* was prepared in deionized water at the desired optical density (OD) as described in Tobler et al. (2011). Note that the OD was measured spectrophotometrically at a wavelength of 600 nm, using 1-cm path length cuvettes. In all experiments, a staged,

horizontal injection approach was chosen, where the *S. pasteurii* suspension was injected first (1 or 7 pore volumes, depending on OD, Table 1) to ensure an even distribution of *S. pasteurii* cells along the cores before cementation started. The rock cores were then left static (i.e., no flow) for 2 hr to allow the microbes to attach to the mineral surfaces. During the second stage, cementation fluid containing 1 mol/L $CaCl_2$ and 1mol/L urea was injected and then the flow was stopped. The fluids in the rock cores were allowed to react until the next day to ensure maximum yield in terms of ureolysis and $CaCO_3$ precipitation, before the cores were flushed with deionized water and the backpressure was measured. Then, this staged injection procedure was repeated daily until substantial clogging occurred, that is, when the backpressure reached approximately 350–450 kPa in the sandstone cores and 1,700 kPa in the fractured granite cores. The injection flow rate was 1 ml/min for the sandstone cores, and 0.5 ml/min for the fractured granite cores, resulting in an average fluid velocity of 0.23 m/hr in the sandstone and a fracture fluid velocity of 2.78 m/hr in the granite. These were based on previous *S. pasteurii* transport and MICP fracture studies (El Mountassir et al., 2014; Tobler et al., 2014) that indicated high bacterial retention at these velocities. At the end of the cementation process the rock cores were thoroughly flushed with deionized water to remove any dissolved salts. The cores were dried at 40 °C until the weight of the cores reached a constant mass (~24 hr). We did not expect any mineralogical changes as a result of this drying at low temperature as the main mineral phases were quartz, feldspar, mica, amphibole and calcite.

In a previous study using packed sand columns (Tobler et al., 2012), a saline solution ($CaCl_2$) was injected parallel with the bacterial suspension to enhance bacterial immobilization, this approach was also applied here in one of the sandstone experiments (SS3 in Table 1). The $CaCl_2$ solution enhances bacterial flocculation (Figure S1 in the supporting information) and hence filtration of the bacteria when injected into a porous matrix.

2.3. BSE Imaging of $CaCO_3$ Distribution

All sealed sandstone cores and one of the sealed fractured granite core (FG1) were embedded in epoxy resin to be cut and polished for backscattered electron (BSE) imaging. The sandstone cores were halved along the long axis and then cut into smaller sections. For the granite core, three parallel cuts were made perpendicular to the fracture plane. The rock sections were polished and analyzed by BSE imaging (Zeiss Sigma Field-Emission Scanning Electron Microscope) as detailed in Tobler et al. (2012). In short, the area for calcite and empty pore space was mapped out using the INCA software package (Oxford Instruments, UK), from which the percentage (by area) of the initial pore space that became filled by $CaCO_3$ was calculated (calcite fill, %). Note that the sandstone and granite cores did not contain any significant amount of $CaCO_3$ grains prior to experimentation as verified by BSE imaging of the untreated sandstone and granite.

2.4. X-CT) Analysis of $CaCO_3$ Distribution

To enable 3-D visualization of the distribution of precipitated $CaCO_3$ within the sealed fractured granite prior to shear testing, X-Ray-Computed Tomography (X-CT; Nikon Metrology) was performed on granite cores, FG2, FG3, and FG4. Relevant scan settings were: resolution of 25 μm, X-ray energy of 170 kV, and 64 μA, exposure time of 1,000 ms, with no prefiltration of the X-ray beam. Each scan consisted of 3,141 projections at angular intervals of 0.114° and were reconstructed with CT PRO 3-D (Nikon Metrology). Beam hardening artifacts were minimized utilizing an automatic beam-hardening correction for single material samples. All further image processing was performed with the FIJI distribution of ImageJ (Schindelin et al., 2015).

A map of the fracture aperture for the fractured granite cores was created by (1) applying a global threshold to the attenuation values (all voxels above the threshold were assumed to be solid, all voxels below the threshold were assumed to be pore space with Otsu's algorithm (Otsu, 1979) used to systematically set the threshold for each scan), (2) removing all solid voxels, (3) removing all pore space voxels not connected to the main fracture body (mostly voids within the granite itself), and (4) counting pore space voxels perpendicular to the fracture plane. This allows 3-D visualization of the $CaCO_3$ precipitated within the fracture as a result of MICP treatment. Further information and a sensitivity analysis on the thresholding procedure used is presented in the supporting information (Figure S2).

Table 1
Comparison of MICP Efficiency Between Sandstone (SS1-SS3) Experiments

Exp.	OD	Bacterial Inj. (PV)[a]	1 M $CaCl_2$ & urea (PV)[a]	# treat-ments	Inj. Ca^{2+} (g)	$CaCO_3$ ppt. (g)	Yield (%)	Filled pore space (%)[b]	Permeability after MICP (cm^2)
SS1	0.15	7	1	13	9.6	16.3	68	32	<1.2E-11
SS2	1.0[c]	1	1	20	14.8	21.1	57	41	2.7E-11
SS3	1.0 + fixative[d]	1	1	11	8.1	14.9	73	30	3.5E-11

[a]Initial pore volume of untreated sandstone core was 18.5 cm^3. [b]Determined by weighing cores before and after plugging (in dry condition). [c]OD was lowered to 0.5 once a backpressure of 15 kPa was reached (i.e., 9 injections with OD = 1 and 11 with OD = 0.5). [d]A 50 mM $CaCl_2$ was used as a fixative.

2.5. Direct Shear Tests of MICP Sealed Granite Fractures

After X-CT scans were acquired, the shearing behavior of the three cores (FG2, FG3, and FG4, Figure S3a) was investigated using a direct shear test (Controls Group) and in accordance with ASTM D5607–16 (2016). The cores were first vacuum saturated in deionized water. Each core was then mounted into the shear box such that the fracture was aligned with the shear plane (Figure S3b). The upper half of the core was cast in place first, using a high strength gypsum plaster (Crystacast, compressive strength of 55.2 MN/m^2) as shown in Figure S3b. Grooves were etched onto the ends of each of the cores to promote attachment with the gypsum plaster (Figure S3a). Once the plaster had dried, the core was inverted, with the upper half now on top, the lower half was cast in the plaster. Vertical alignment was ensured by using two alignment screws (Figure S3c). After approximately 20 hr curing time, the upper and lower halves of the shear box containing the core could be placed in the direct shear equipment (Figure S3d).

The cores were fully submerged prior to shearing. A vertical stress of 150 kPa was applied. A constant horizontal displacement rate of 1.00 mm/min was applied for FG3. As this resulted in the peak shear strength being reached within a very short time period (~10 s) the horizontal displacement rate was reduced to 0.2 mm/min for the testing of FG2 and FG4. Measurements were acquired at a frequency of 0.44 Hz.

After shearing of the sealed granite fractures, the vertical load and upper half of the shear box were removed, the fracture surfaces were air dried and photographed. All $CaCO_3$ precipitate was then dissolved by exposing the fracture surface only to 3.7% hydrochloric acid for approximately 2 hr. Afterward, the shear box was reassembled to measure the residual shear strength of the clean granite surfaces using the same approach as above and shown in Figure S3.

3. Results and Discussion

In all experiments discussed below *S. pasteurii* suspensions were injected without the addition of any nutrients, in order to minimize bacterial growth inside the cores (also demonstrated by time-dependent OD measurements of the suspensions, Figure S1). The only reagents used were 1 M urea and 1 M $CaCl_2$ to keep the system as simple as possible. This is in contrast to most previous studies that have investigated the use of MICP for sealing pores and fractures in rocks (Cunningham et al., 2014; Kirkland et al., 2017; Phillips et al., 2013, 2016). In terms of field application, the applied staged approach (with static flow conditions in between) would be suitable for MICP treatment in subsurface porous and fractured rock, where ambient groundwater flow rates are minimal (<1 mm/day), for example, oil reservoir, aquifer, and deep geologic storage sites for nuclear waste and CO_2.

3.1. Sandstone Cores

The injection strategy for achieving a homogeneous calcite distribution was first investigated in sandstone cores, as this rock system is more similar to the sand columns systems, which have been extensively studied to date. Three Bentheimer sandstone cores were used to test (1) the effect of bacterial density and (2) the addition of a bacterial fixative, on MICP distribution along the sandstone core and on the number of injections required to reduce the permeability by ~3 orders of magnitude, to $\leq 3.5 \times 10^{-11}$ cm^2 (i.e., ≥350 kPa backpressure). Note that the number of injected bacterial cells per treatment cycle was similar in these three experiments.

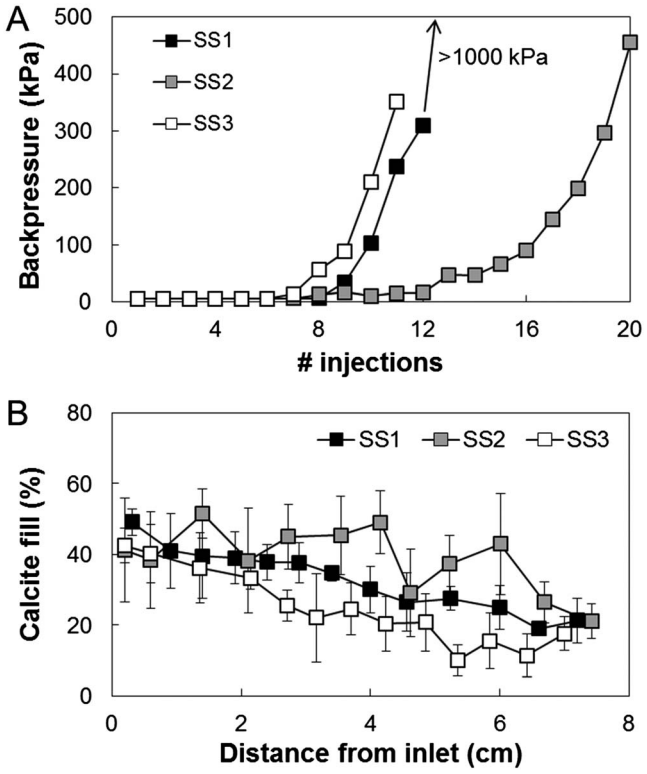

Figure 1. (a) Backpressure increase as a result of pore space plugging by calcite in sandstone experiments. Targeted posttreatment permeability $\leq 3.5 \times 10^{-11}$ cm^2 corresponds to a backpressure increase of ≥350 kPa. (b) Distribution of calcite fill along the length of the sandstone cores at the end of the experiment as determined by BSE imaging (section 2.3). BSE = backscattered electron.

In the SS1 experiment, where a low cell density of bacteria (OD = 0.15) was injected for about 2 hr in each cycle (7 PV), the targeted permeability reduction was reached after 13 cycles of bacterial and reagent injection (Figure 1a), with microbially precipitated calcite filling 32% of the initial pore space (Table 1). In comparison, in the SS2 experiment, where just one pore volume of bacterial suspension, but at a higher cell density (OD = 1.0), was injected, it required 20 reagent injections (i.e., seven more) to achieve a similar 3 orders of magnitude reduction in permeability, with calcite filling 41% of the initial porosity (Table 1). Comparison of the calcite distribution along these two cores (Figure 1b) shows that for SS2, the calcite fill is homogeneous, fluctuating around 40%, while for SS1, it decreases steadily from 50% at the inlet to about 20% at the outlet. Thus, the use of a lower bacterial density, but multiple pore volumes in SS1 led to a faster permeability reduction and a higher overall reaction yield (i.e., injected vs precipitated Ca; Table 1), but at the cost of blocking pores closer to the inlet. Instead, injecting one pore volume of a high cell density suspension, led to a more homogeneous and overall higher percent of calcite fill but required more time and reactants to reduce the permeability to $\leq 3.5 \times 10^{-11}$ cm^2 (SS2 in Table 1). These results were unexpected because bacterial distribution (and therefore calcite fill) was expected to improve when the bacteria were injected at lower OD due to a lower risk of saturating attachment sites for bacteria (Tobler et al., 2014). However, injection of multiple pore volumes of bacteria may potentially have increased bacterial aggregation due to forced mixing of existing bacteria cells in the pore fluid with cells in subsequent pore volumes, thus enhancing overall bacterial retention; this may have had more of an influence toward the inlet.

In a third sandstone experiment (SS3), a bacterial fixative (50 mM $CaCl_2$) was injected parallel with the bacterial suspension (Table 1). The use of the fixative promotes aggregation of the bacteria (Figure S1), which contributes to enhanced retention of bacteria within the sandstone core during bacterial injections. Tobler et al. (2014) showed that 24% of injected *S. pasteurii* cells when suspended in deionized water passed through a sandstone core, while <1% were recovered when suspended in 50 mM $CaCl_2$ solution (for the same flow conditions; Figure S4). In this experiment, only 11 treatment cycles were required to reach the targeted permeability reduction (Table 1). However, the calcite fill along the core was the most heterogeneous among the three tested approaches (Figure 1b), with calcite filling 30% of the initial pore space. Considering the low number of injections, a calcite fill of 30% is substantial, also shown by the high reaction yield of 73% (Table 1).

Overall, the results from these experiments showed that *S. pasteurii* cells yield high ureolytic activity within the sandstone matrix, similar in extent to that observed in sand columns using this very same staged injection approach (Tobler et al., 2012). If a $CaCl_2$ solution (fixative) is injected in parallel with the bacterial suspension, a larger number of cells can be immobilized within the sandstone matrix. The presence of a fixative promotes flocculation (Figure S1); however, bacterial filtration along the sandstone core appears to be heterogeneous, with more cells becoming trapped within the first few centimeters, which eventually leads to the observed heterogeneous calcite pore space fill. It is important to note that the same approach was previously applied to sand columns but the distribution of calcite fill along the length of the core was more homogeneous when a bacterial fixative was used (Tobler et al., 2012). This supports our previous observation in that it is difficult to compare processes in consolidated rock with processes in sand column experiments, because rock characteristics, for example, wider grain size distribution, smaller pore spaces and throats, and higher abundance of dead-end pores, can impact bacterial transport (Tobler et al., 2014) and thus the location where calcite is precipitated. In terms of field application, the use of a bacterial fixative may not be suitable for treating large rock volumes in the subsurface. However, in a situation where a seal is required near the injection point, this approach (of those tested) seems to be the most rapid and cost-effective.

A more homogeneous calcite fill developed when no fixative was used (SS2 core). Our initial hypothesis that the injection of multiple pore volumes of low density bacterial suspensions could improve bacterial distribution as determined previously (Tobler et al., 2014), and hence the calcite fill, proved incorrect. A comparison of the results for SS1 and SS2 suggests that injection of the considered bacterial mass in one single pore volume in sandstone may yield a more homogeneous calcite fill, rather than the injection of multiple pore volumes of a more dilute bacterial suspension. It is important to note that the precipitation of $CaCO_3$ quickly changes the size and distribution of pore spaces and throats, pore surface reactivity, and flow dynamics within the rock. Thus, once more bacteria are injected into this modified matrix, the bacterial distribution and percent recovery will likely be substantially different compared to the initial injection (Tobler et al., 2014).

Based on the results in Table 1, the injection strategy used in SS2 was selected for application in the following experiments in the fractured granite cores. It is recognized that the flow within a porous rock is different from the 2-D planar flow conditions within a smooth rock fracture. For example, there is little straining of bacteria in a smooth fracture, which will result in reduced bacterial retention and hence calcite nucleation. However, as calcite crystals nucleate and grow at multiple locations on the fracture surfaces, the flow pathways within a fracture will become more tortuous, tending toward those found within porous rocks.

3.2. Fractured Granite

3.2.1. Calcite Distribution in Fractured Granite Cores

The granite cores had artificially created smooth fractures with an initial aperture of approximately 300 μm. After 17 treatment cycles, the transmissivity in FG1 was reduced from 7.1×10^{-7} to 3.2×10^{-11} m^2/s. BSE examination of the cut FG1 core (Figure 2a) showed that calcite precipitated evenly on both fracture surfaces (Figures 2b–2d). In several parts, calcite bridged across the two fracture surfaces, filling the aperture completely (Figures 2b, 2e–2g). Close-up analysis of the calcite fill showed that the calcite grew perpendicular to the fracture plane, with each treatment cycle generating a layer of calcite. Each calcite layer is delineated by cavities with diameters ~0.5–1 um (cross section of a bacterial cell), which mark locations where bacteria became embedded (Figures 2g–2j). This is shown in Figures 2j, S4a, and S4b, where the spherical and rod-shaped cavities match the dimensions of *S. pasteurii* cells. The trapping of bacterial cells within the calcite precipitate, thereby leaving characteristic bacterial-shaped cavities within the crystals, has also been demonstrated in previous MICP studies (e.g., Mitchell & Ferris, 2005; Skuce et al., 2017; Tobler et al., 2012; Warren et al., 2001).

The calcite layers that are seen here range in thickness between 4 and 10 μm, with an average thickness of 6.6 ± 2.3 μm (Figures 2 and S5). Moreover, layers did not progressively become thicker or thinner with each injection cycle but appeared to maintain an average thickness of around 6.6 μm throughout the experiment. This element of consistency may facilitate development of fracture filling models based upon fracture thickness and geometry. For example, with an average layer thickness of 6.6 μm growing from both walls, it would take just over 23 injection cycles to plug the 300 μm (perfectly smooth) fracture. This is not far off the 17 injection cycles it took to significantly reduce permeability. Indeed, while layer growth shows an element of consistency, it is not identical in all areas; hence, at some locations calcite layers build up faster than others; hence, less than 23 injection cycles are required to significantly reduce permeability. Interestingly, these findings are consistent with the layered buildup of calcite seen in MICP treated packed sand columns where a similar staged approach was used and where the calcite layers exhibited a very similar thickness and variability (Tobler et al., 2012). Another interesting aspect concerns the morphology of the calcite crystals, which are sometimes rounded, particularly when looking at the very first $CaCO_3$ layer that formed on the fracture surface (dashed lines marked by arrows in Figures 2f and S5d). This could indicate that some vaterite might have also formed and then was later replaced by calcite.

An estimate of the percent fracture space filled by calcite was obtained by area measurements from lower-resolution BSE images (e.g., Figures 2b–2d). This showed that about 67 ± 22% of the fracture was filled with calcite. This indicates that a fairly high percent fill is required to hydraulically seal this homogeneous fracture, with perfectly smooth surfaces, which is unlike a real fracture. The observed variability in calcite fill could not be linked to any geometric position in the core (i.e., close or distant to inlet or core center) nor any microstructural differences along the fracture (i.e., pits and hillocks on the granite surface). Similarly, the varying mineralogy on the fracture surface (e.g., quartz, feldspar, amphibole, mica) did not seem to affect the sites where calcite (and possibly vaterite) crystals formed (Figures 2b–2d and S6).

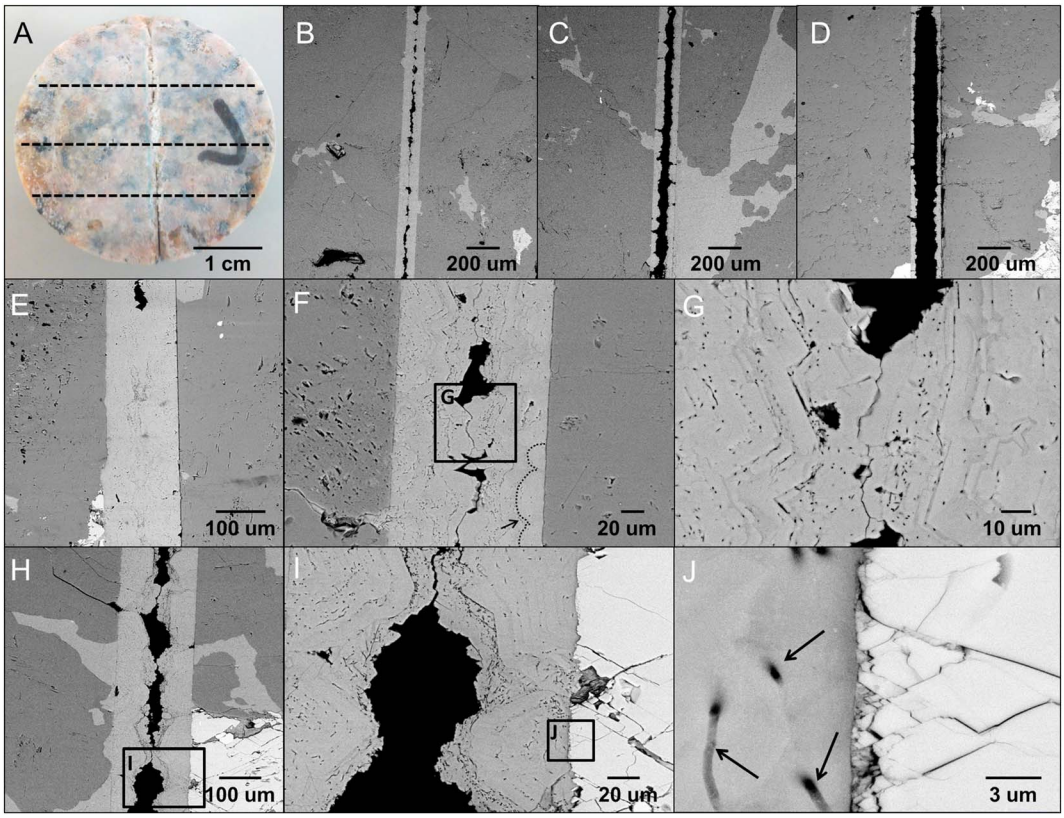

Figure 2. (a) Photographic image of the treated granite core (top view) with the dashed lines showing where it was cut into three pieces for backscattered electron (BSE) imaging of the fracture profile. A representative set of BSE images and observations gathered from these three sections are shown in (b)–(j). (b–d) BSE images giving the fracture profile showing calcite precipitate on both fracture planes, with the amount varying across the fracture plane with no visible dependence on fracture surface mineralogy, that is, surface properties (highlighted by different contrast in BSE images) or location on the fracture. (e–i) At several places, the calcite bridged across both fracture surfaces (i.e., calcite filled the aperture); also showing how the precipitate grew from the fracture planes toward the middle. The calcite fill shows characteristic micro-stromatolitic textures (G&I), where calcite growth layers are marked by ~0.5 um cavities (black dots, at times more rod-shaped) that mark locations where bacterial cells were embedded. (j) Close-up of (i), showing cavities left by embedded bacterial cells (indicated by arrows). It also shows that little cracks on the fracture surface are filled with calcite precipitate.

Cores FG2, FG3, and FG4 were imaged (nondestructively) using X-CT prior to testing their shear strength. X-CT has a lower resolution (25 μm) compared to the nanometer-scale resolution of BSE images shown in Figure 2 for FG1, but allows 3-D imaging and the creation of *virtual thin sectioning* of any point in the sample. This is shown in Figure 3a, where low-density pore space is shaded blue to black and higher-density granite minerals and calcite are shaded orange to white. Maps of the fracture aperture variation for cores FG2, FG3, and FG4 are shown in Figure 3b. The fracture aperture after treatment varies from 0 μm (shown in white, below the scan resolution of 25 μm), where calcite now fills the fracture, to 300 μm (shown in black), that is, the initial fracture aperture where no calcite has precipitated. It is evident that calcite precipitated across most of the fracture plane, indicated by the reduction in fracture aperture after treatment, from its initial value (Figure 3b). There are numerous small voids and a single large void shown in FG2 where no calcite precipitation is present. It also appears that more sealing occurred at the top and bottom boundaries of each core (indicated in white in Figure 3b). For details regarding the uncertainty associated with segmenting X-CT scans into solid and pore phases, the readers are directed to Figure S2 in the supporting information.

Regions where calcite has bridged across the two fracture surfaces were defined as any point in the fracture aperture map where aperture was <25 μm, as shown in Figure 3c. For FG3, only 8.9% (by area) of the fracture was bridged with calcite, with the majority of that located at or in close proximity to the top and bottom boundaries of the core. In contrast, 15.9% and 13.5% (by area) of the fracture was bridged in the FG2 and FG4 core. Despite having a larger percent area of calcite bridging across the two fracture surfaces, FG2 and

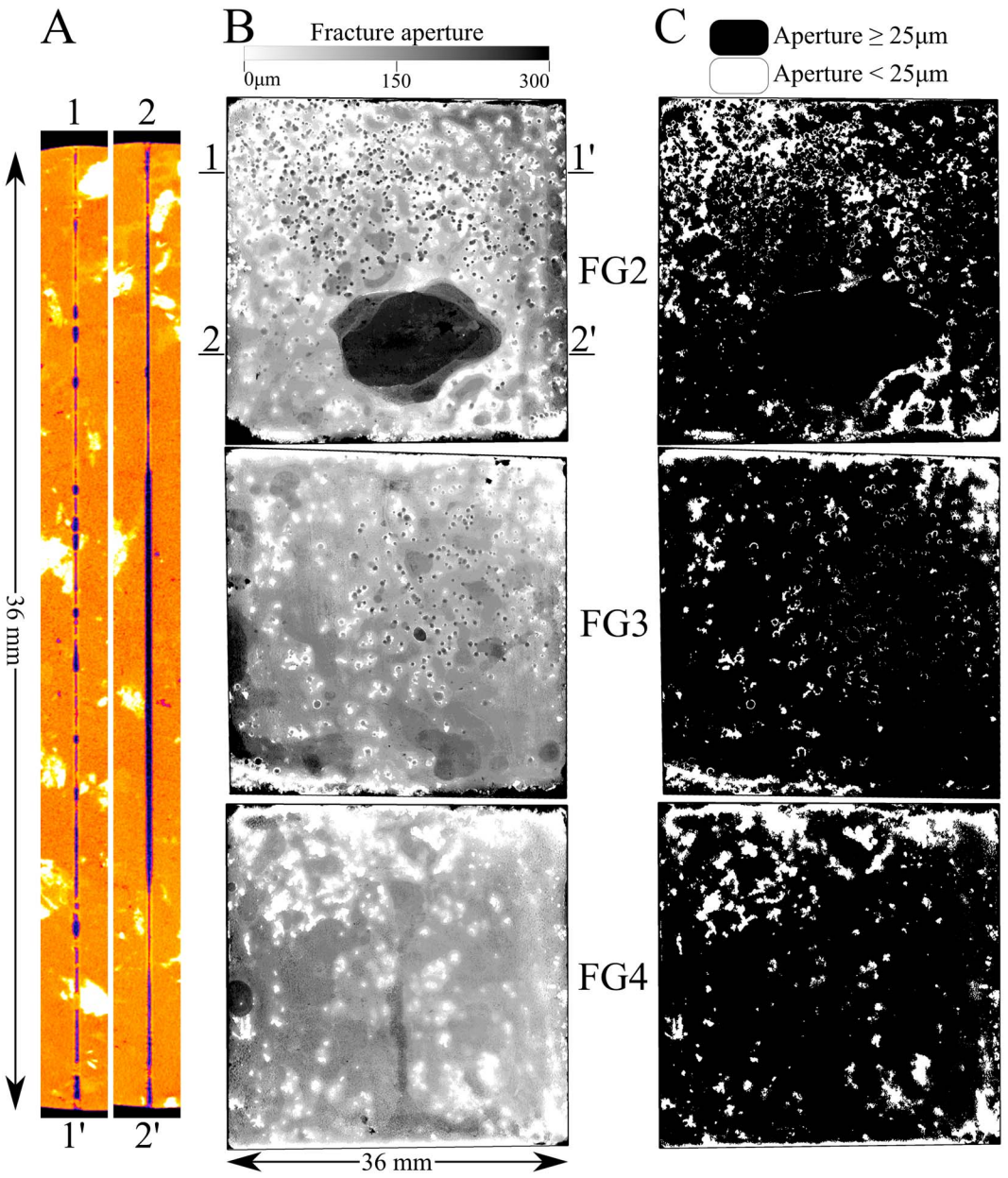

Figure 3. X-CT results and analysis. (a) X-ray attenuation in two representative slices through sample FG2. After binary segmentation of the X-ray attenuation data into solid and pore space, (b) 2-D representation of aperture variation (given by the gray scale) across the 36 × 36 mm fracture plane, and (c) highlight of where $CaCO_3$ bridges the two fracture surfaces (white) and where there is at least one voxel of pore space (black), as far as discernible with the X-ray resolution of 25 μm. Flow direction during treatment was into the page for (a) and along the vertical axis for (b) and (c).

FG4 had a higher permeability after treatment than FG3 (Table 2). The very low permeability determined for FG3 after MICP treatment is likely due to the almost complete sealing of the inlet boundary (at the top of the image in Figure 3b, FG3), indicating that it is both the amount of $CaCO_3$ and its distribution within the fracture that determines permeability reduction. This in turn suggests that to produce a long-lasting permeability reduction in a subsurface fracture using MICP, it is desirable to precipitate $CaCO_3$ more uniformly over a larger area (as occurred in FG2 and FG4).

Cores FG2 and FG3 contained numerous small spherical voids within the fracture fill where no calcite was observed (about 500 μm in diameter, Figure 3b and close-ups shown in Figure S7). Often these were accompanied by an outer ring with no discernible pore space. These voids are consistent with the presence of gas

Table 2
Fractured Granite Core Results. MICP Treatments for the Four Fracture Granite Cores (FG1-FG4) Were Identical

Exp.	# treatments	Pore volume (cm^3)	Transmissivity after MICP (m^2/s)[a]	Average fracture aperture after MICP (μm)	% of fracture area bridged with calcite[c]	Peak shear strength (kPa)	Residual shear strength (kPa)
FG1	17	0.39	3.2E−11	98 ± 66[b]		-	-
FG2	16	0.39	1.2E−08	109[c]	15.9	484	114
FG3	16	0.39	9.7E−11	118[c]	8.9	125	125
FG4	16	0.39	4.4E−09	112[c]	13.5	733	109

Note. Following sealing, FG1 was used for BSE characterization (section 2.3) and FG2–FG4 were characterized by X-ray CT and used for shear strength testing (sections 2.4 and 2.5). MICP = Microbially induced $CaCO_3$ precipitation.
[a]Average initial transmissivity of the fractured granite cores was 7.1×10^{-7} m^2/s. [b]Estimated by measuring the % fracture area filled by calcite in 15 BSE images (e.g., Figures 3b–3d). The error represents one standard deviation. [c]Determined from fracture aperture map (Figure 3c) created from X-CT scans. Figure S2 shows sensitivity of these values as a function of threshold value used during image segmentation.

bubbles that may have become encased in a $CaCO_3$ shell as sealing progressed. FG2 featured a single large void within the fracture after sealing where no $CaCO_3$ was detected. FG4 contained no obvious small voids and a single void 3.75 mm in diameter.

3.2.2. Fractured Granite Shear Strength

Figure 4 presents the shearing results of the fractured granite cores, after MICP treatment (FG2-CaCO3 to FG4-CaCO3) and after all the calcite was removed by acid (FG2-no fill to FG4-no fill). After MICP treatment all cores showed an increased resistance to shearing indicated by the initially steeper curve in the shear stress–horizontal displacement plot, compared to the same fractures with no fill present (Figure 4). FG3 exhibited a peak shear strength of 125 kPa, whereas FG2 and FG4 exhibited higher peak shear strengths of 484 and 733 kPa with corresponding brittle failure (i.e., a rapid drop in shear strength at failure, Figure 4). For each MICP treated core, the residual shear strength measured after failure had occurred was higher than the residual shear strength measured for the same fracture with no calcite (i.e., untreated granite fracture, dotted lines in Figure 4). This is likely due to $CaCO_3$ precipitates increasing the roughness of the fracture surfaces (Figures 2 and 3) contributing to an increase in shear resistance compared to the untreated granite surfaces.

Examination of the fractured surfaces of FG2 to FG4 postshearing (Figure 5) shows that calcite coated the granite on both fracture surfaces evenly, indicating that failure occurred within the $CaCO_3$ biogrout, as opposed to that at the contact between the grout and the granite rock. This indicates that the calcite is very strongly attached to the granite rock; an observation also supported by the strongly attached calcite fill in the BSE images (Figures 2J and S6). In contrast, it has been reported that failure in cement-grouted fractures occurs at the cement-rock interface (Coulson, 1970 for low normal stresses <800 kPa) or close to the cement-rock interface (Swedenborg & Dahlström, 2003). The difference in failure location may arise from the two different processes by which the grout forms: $CaCO_3$ crystal growth requires progressive growth on nucleation sites provided by the surface attached bacteria (Dupraz et al., 2009; Stocks-Fischer et al., 1999), the rock itself, or previously precipitated $CaCO_3$ (also attached to a surface); whereas cement hydration takes place on internal nucleation sites and results in volumetric shrinkage (Scherer et al., 2012) which is likely to lead to poorer attachment on smooth surfaces. It is important to note that the shear strength of MICP treated fractures could potentially be further enhanced by injecting more treatment cycles (permeability permitting) or tailoring the injection strategy to promote further calcite bridging occurring across the entire fracture aperture. In contrast, cement grout failure due to shearing is governed by the strong contrast in material properties existing at the cement-rock interface, thus little can be done to improve their adhesive bond to the rock surface.

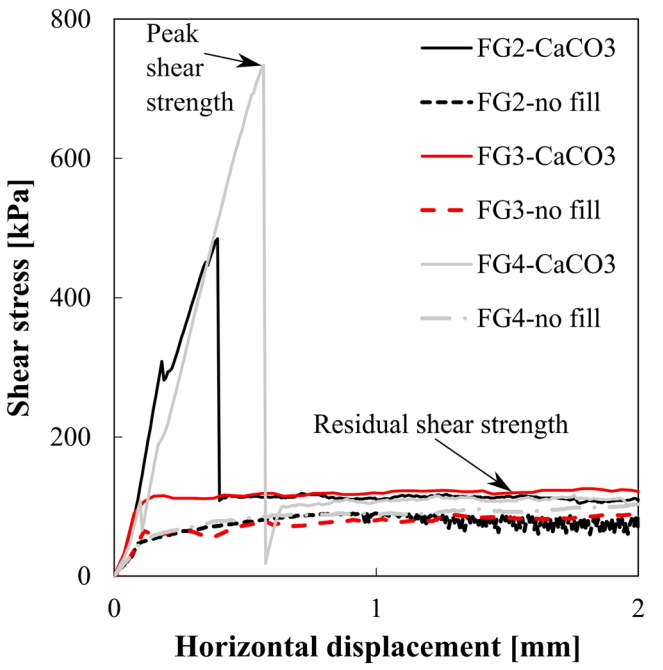

Figure 4. Direct shear results for fractured granite cores treated with Microbially induced $CaCO_3$ precipitation, and for the fractures with no fill after removal of $CaCO_3$ (i.e., untreated fractures).

The peak shear strength appears to correlate well with the distribution of calcite as determined with X-CT prior to shearing (Figure 3). FG2 and FG4

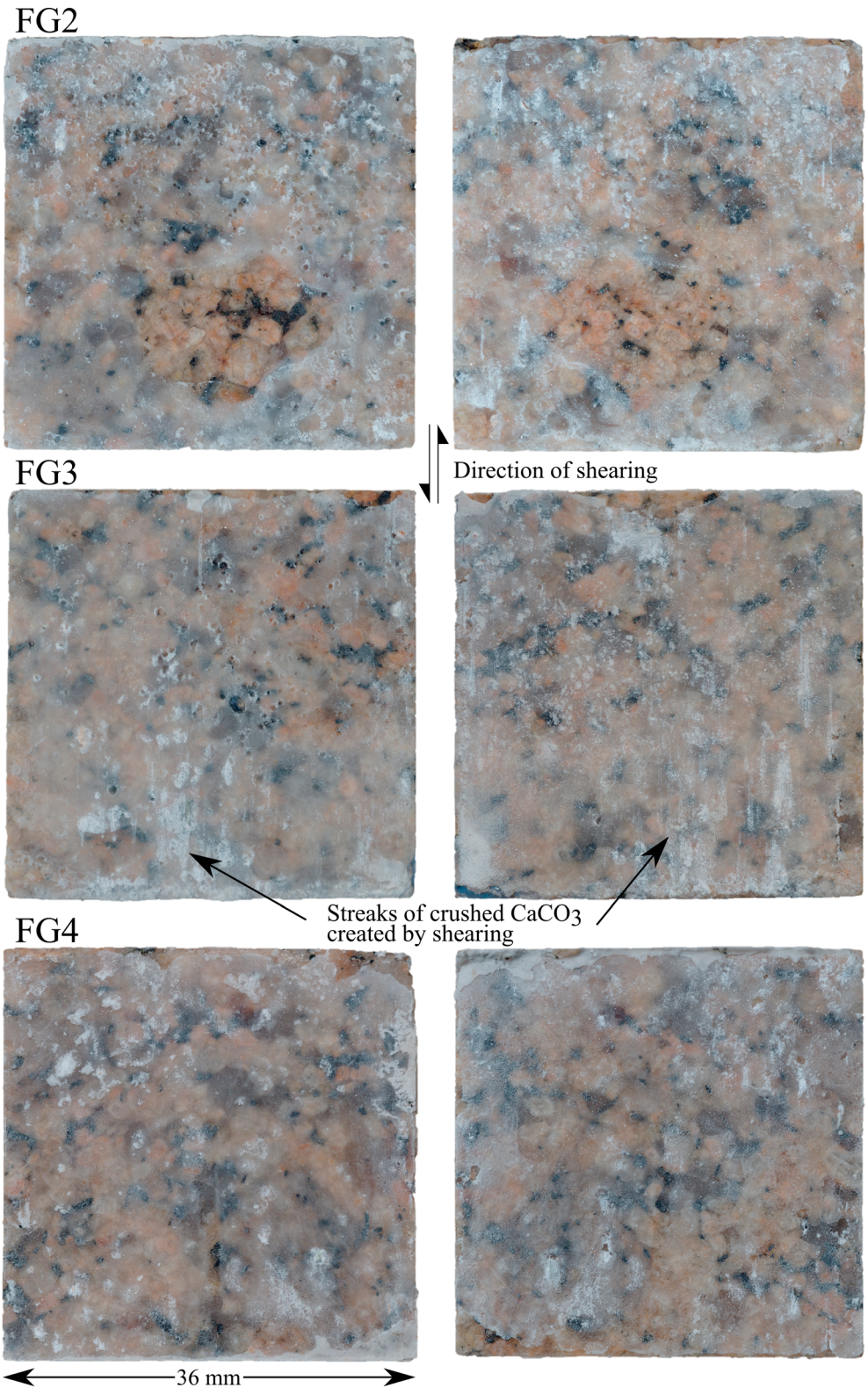

Figure 5. Photographic image of both fracture surfaces after shearing, rinsing, and drying. White $CaCO_3$ (i.e., calcite) is visible on both surfaces (except where gas bubbles might have been present) and includes streak lines of crushed calcite in the direction of shearing. Loose calcite powder created by shearing was removed by gently rinsing with tap water and is therefore not shown in the photographs. The two fracture halves are presented as if opened like a book, and the left column has been orientated so as to match the fracture aperture maps of Figure 3.

had a higher percentage of the fracture area where calcite bridged across both fracture surfaces compared to FG3 (Table 2). The degree of calcite bridging likely contributed to the measured peak shear strength. In turn, the brittle response we observed may be explained by the failure of the grout at these bridging points. FG4 exhibited a higher peak shear strength than FG2, despite having a slightly lower percent of the fracture completely filled by calcite. This may be because the patches of calcite bridging the aperture are larger for FG4 than in FG2 where the calcite bridges consist of many small disconnected points. Furthermore, FG2 contains a large void which will likely have weakened its mechanical behavior (Figures 3b and 4). The lower peak shear strength measured for FG3 may also be partly attributed to the higher shearing rate used (1 mm/min, compared to 0.2 mm/min for FG2 and FG4). It should also be noted that FG2 and FG4 had a higher permeability than FG3 after treatment with MICP. The X-CT images in Figure 3 indicate that this was due to the higher amount of calcite precipitates present at the boundaries of FG3, whereas FG2 and FG4 had a more evenly distributed calcite fill.

4. Conclusions

Initial core tests in porous sandstone indicated that the use of a high-density bacteria solution in the absence of a fixative resulted in the most homogeneous calcite distribution. This approach was then used for treating fractured granite cores. Tests show that MICP treatment reduced fracture transmissivity by up to 4 orders of magnitude. However, this required a substantial number of treatment cycles, 16 or 17 cycles for each core (Table 2). This is not surprising as the granite fractures were created artificially, with very smooth fracture surfaces and a constant initial aperture. Thus, they required many treatment cycles as they contained no narrow pore throats to facilitate clogging. Treatment of a subsurface fracture would likely require less treatment cycles to reduce its permeability to such an extent. This is because natural fractures are heterogeneous. For example, they have varying geometry (surface roughness, abrupt changes in aperture, width, branching) and they often also contain inorganic (e.g., clay fill) or organic (e.g., biofilms) surface coatings. These factors can act to enhance bacterial immobilization on fracture surfaces, promote calcite growth, and also lower the amount of calcite growth required to completely close up the fracture.

MICP treatment significantly increased the resistance of the fractures to shearing. Grout materials which enhance mechanical as well as hydraulic behavior are desirable for engineering contexts where stress distributions are anticipated to change. This may include short-term applications like excavations and tunneling where pregrouting has been carried out, or long-term applications such as the deep geological disposal of nuclear waste. The microscopic evaluation of calcite distribution carried out in this paper suggests that a major factor in achieving a high shear strength is the spatial distribution of calcite crystals that bridge across both fracture surfaces, completely filling the fracture aperture. In natural systems these bridging points are likely to form more quickly and possibly be more extensive due to existing contact points, as a result of natural fracture roughness and existing fracture fill. If shearing of MICP grouted fractures does occur in situ, there is also the potential that any cracks formed may self-heal, without the reintroduction of further bacteria to the system (Montoya & Dejong, 2013).

When grouting fine aperture fractures for hydraulic sealing, MICP is a promising grout material. The small size of the bacteria and low viscosity of the treatment solutions give it excellent penetrability compared to traditional cement grouts. Moreover MICP has been shown here to enhance shearing resistance with excellent adhesion to artificially smooth granite fracture surfaces, with failure only occurring within the MICP biogrout itself. If treatment strategies can be designed such that both fracture surfaces are bridged by precipitated $CaCO_3$, then MICP grouted fractures have the potential to provide additional mechanical stability to a rock mass as well as providing a hydraulic barrier. Calcite is known from natural analogs to be durable over geological timescales, whereas cement grouts are known to degrade over timescales ~100 years, with increasing porosity negatively influencing their hydraulic and mechanical performance, such that progressive degradation can result in cement barriers acting as flow paths (Laver et al., 2013).

Acknowledgments
This work was funded by an Engineering and Physical Sciences Research Council (EPSRC) grant (EP/G063699/1) and EPSRC Big Pitch grant EP/M016854/1. All data used in this study are publicly available from the University of Strathclyde data repository http://dx.doi.org/10.15129/0f92623e-df99-4caf-9734-61cacb235913

References

ASTM D5607-16 (2016). Standard test method for performing laboratory direct shear strength tests of rock specimens under constant normal Force.

Bodén, A., & Sievänen, U. (2005). Low-pH injection grout for deep repositories, SKB report R-05-40/Posiva Report WR 2005-24.

Coulson, J. H. (1970). The effects of surface roughness on the shear strength of joints in rock (PhD thesis). University of Illinois at Urbana-Champaign, USA.

Cunningham, A. B., Phillips, A. J., Troyer, E., Lauchnor, E., Hiebert, R., Gerlach, R., & Spangler, L. (2014). Wellbore leakage mitigation using engineered biomineralization. *Energy Procedia*, *63*, 4612–4619. https://doi.org/10.1016/j.egypro.2014.11.494

Cuthbert, M. O., McMillan, L., Handley-Sidhu, S., Riley, M. S., Tobler, D. J., & Phoenix, V. R. (2013). A field and modelling study of fractured rock permeability reduction using microbially induced calcite precipitation. *Environmental Science & Technology*, *47*(23), 13,637–13,643. https://doi.org/10.1021/es402601g

Dejong, J. T., Soga, K., Kavazanjian, E., Burns, S., van Paassen, L. A., Al Qabany, A., & Weaver, T. (2013). Biogeochemical processes and geotechnical applications: Progress, opportunities and challenges. *Geotechnique*, *63*(4), 287–301. https://doi.org/10.1680/geot.SIP13.P.017

Dupraz, S., Parmentier, M., Ménez, B., & Guyot, F. (2009). Experimental and numerical modeling of bacterially induced pH increase and calcite precipitation in saline aquifers. *Chemical Geology*, *265*(1-2), 44–53. https://doi.org/10.1016/j.chemgeo.2009.05.003

El Mountassir, G., Lunn, R. J., Moir, H., & McLachlan, E. (2014). Hydrodynamic coupling in microbially mediated fracture mineralization: Formation of self-organized groundwater flow channels. *Water Resources Research*, *50*, 1–16. https://doi.org/10.1002/2013WR013578

Ferris, F. G., Phoenix, V., Fujita, Y., & Smith, R. W. (2003). Kinetics of calcite precipitation induced by ureolytic bacteria at 10 to 20°C in artificial groundwater. *Geochimica et Cosmochimica Acta*, *67*, 1701–1722.

Ferris, F. G., & Stehmeier, L. G. (1992). Bacteriogenic mineral plugging, Patent [5,143,155], U.S. Pat. Off., Washington, DC.

Kirkland, C. M., Zanetti, S., Grunewald, E., Walsh, D. O., Codd, S. L., & Phillips, A. J. (2017). Detecting microbially induced calcite precipitation in a model well-bore using downhole low-field NMR. *Environmental Science & Technology*, *51*(3), 1537–1543.

Laver, R. G., Soga, K., Wright, P., & Jefferis, S. (2013). Permeability of aged grout in tunnels around London. *Géotechnique*, *63*(8), 651–660. https://doi.org/10.1680/geot.11.P.125

Minto, J. M., El Mountassir, E., Mountassir, G., & Lunn, R. J. (2016). Rock fracture grouting with microbially induced carbonate precipitation. *Water Resources Research*, *52*, 8827–8844. https://doi.org/10.1002/2016WR018884

Minto, J. M., Hingerl, F. F., Benson, S. M., & Lunn, R. J. (2017). X-ray CT and multiphase flow characterization of a 'bio-grouted' sandstone core: The effect of dissolution on seal longevity. *International Journal of Greenhouse Gas Control*, *64*, 152–162. https://doi.org/10.1016/j.ijggc.2017.07.007

Mitchell, A. C., Dideriksen, K., Spangler, L. H., Cunningham, A. B., & Gerlach, R. (2010). Microbially enhanced carbon capture and storage by mineral-trapping and solubility-trapping. *Environmental Science & Technology*, *44*(13), 5270–5276. https://doi.org/10.1021/es903270w

Mitchell, A. C., & Ferris, F. G. (2005). The coprecipitation of Sr into calcite precipitates induced by bacterial ureolysis in artificial groundwater: Temperature and kinetic dependence. *Geochimica et Cosmochimica Acta*, *69*(17), 4199–4210. https://doi.org/10.1016/j.gca.2005.03.014

Mitchell, A. C., Phillips, A. J., Schultz, L. N., Parks, S. L., Spangler, L. H., Cunningham, A. B., & Gerlach, R. (2013). Microbial $CaCO_3$ mineral formation and stability in an experimentally simulated high pressure saline aquifer with supercritical CO_2. *International Journal of Greenhouse Gas Control*, *15*, 86–96. https://doi.org/10.1016/j.ijggc.2013.02.001

Montoya, B. M., & Dejong, J. T. (2013). Healing of biologically induced cemented sands. *Géotechnique Letters*, *3*(3), 147–151. https://doi.org/10.1680/geolett.13.00044

Otsu, N. (1979). A threshold selection method from gray-level histograms. *IEEE Transactions on Systems, Man, and Cybernetics*, *9*(1), 62–66. https://doi.org/10.1109/TSMC.1979.4310076

Phillips, A. J., Cunningham, A. B., Gerlach, R., Hiebert, R., Hwang, C., Lomans, B. P., et al. (2016). Fracture sealing with microbially-induced calcium carbonate precipitation: A field study. *Environmental Science & Technology*, *50*(7), 4111–4117. https://doi.org/10.1021/acs.est.5b05559

Phillips, A. J., Gerlach, R., Lauchnor, E., Mitchell, A. C., Cunningham, A. B., & Spangler, L. (2013). Engineered applications of ureolytic biomineralization: A review. *Biofouling*, *29*(6), 715–733. https://doi.org/10.1080/08927014.2013.796550

Reid, C., Lunn, R., El Mountassir, G., & Tarantino, A. (2015). A mechanism for bentonite buffer erosion in a fracture with a naturally varying aperture. *Mineralogical Magazine*, *79*(6), 1485–1494. https://doi.org/10.1180/minmag.2015.079.6.23

Rodriguez-Blanco, J. D., Shaw, S., Bots, P., Roncal-Herrero, T., & Benning, L. G. (2012). The role of pH and Mg on the stability and crystallization of amorphous calcium carbonate. *Journal of Alloys and Compounds*, *536*, S477–S479. https://doi.org/10.1016/j.jallcom.2011.11.057

Rodriguez-Blanco, J. G., Sand, K. K., & Benning, L. G. (2017). ACC and vaterite as intermediates in the solution-based crystallization of $CaCO_3$. In A. E. S. van Driessche, M. Kellermeier, L. G. Benning, & D. Gebauer (Eds.), *New perspectives on mineral nucleation and growth* (pp. 93–112). Chambridge: Springer. https://doi.org/10.1007/978-3-319-45669-0_5

Scherer, G. W., Zhang, J., & Thomas, J. J. (2012). Nucleation and growth models for hydration of cement. *Cement and Concrete Research*, *42*(7), 982–993. https://doi.org/10.1016/j.cemconres.2012.03.019

Schindelin, J., Rueden, C. T., Hiner, M. C., & Eliceiri, K. W. (2015). The ImageJ ecosystem: An open platform for biomedical image analysis. *Molecular Reproduction and Development*, *82*(7–8), 518–529. https://doi.org/10.1002/mrd.22489

Sham, E., Mantle, M. D., Mitchell, J., Tobler, D. J., Phoenix, V. R., & Johns, M. L. (2013). Monitoring bacterially induced calcite precipitation in porous media using magnetic resonance imaging and flow measurements. *Journal of Contaminant Hydrology*, *152*, 35–43. https://doi.org/10.1016/j.jconhyd.2013.06.003

Skuce, R. L., Tobler, D. J., MacLaren, I., Lee, M. R., & Phoenix, V. R. (2017). Immobilization of nanoparticles by occlusion into microbial calcite. *Chemical Geology*, *453*, 72–79. https://doi.org/10.1016/j.chemgeo.2017.02.005

Stocks-Fischer, S., Galinat, J. K., & Bang, S. S. (1999). Microbiological precipitation of $CaCO_3$. *Soil Biology and Biochemistry*, *31*(11), 1563–1571. https://doi.org/10.1016/S0038-0717(99)00082-6

Swedenborg, S., & Dahlström, L. O. (2003). Rock mechanics effects of cement grouting in hard rock masses. Grouting and ground treatment. In *Proceedings of the Third International Conference on Grouting and Ground Treatment* (pp. 1089–1102). New Orleans, Louisiana: ASCE.

Tobler, D. J., Cuthbert, M. O., Greswell, R. B., Riley, M. S., Renshaw, J. C., Handley-Sidhu, S., & Phoenix, V. R. (2011). Comparison of rates of ureolysis between *Sporosarcina pasteurii* and an indigenous groundwater community under conditions required to precipitate large volumes of calcite. *Geochimica et Cosmochimica Acta*, *75*(11), 3290–3301. https://doi.org/10.1016/j.gca.2011.03.023

Tobler, D. J., Cuthbert, M. O., & Phoenix, V. R. (2014). Transport of *Sporosarcina pasteurii* in sandstone and its significance for subsurface engineering technologies. *Applied Geochemistry*, *42*, 38–44. https://doi.org/10.1016/j.apgeochem.2014.01.004

Tobler, D. J., Maclachlan, E., & Phoenix, V. R. (2012). Microbially-mediated plugging of porous media and the impact of differing injection strategies. *Ecological Engineering*, *41*, 270–278.

Van Paassen, L. A., Ghose, R., van der Linden, T. J. M., van der Star, W. R. L., & van Loosdrecht, M. C. M. (2010). Quantifying biomediated ground improvement by ureolysis: Large-scale biogrout experiment. *Journal of Geotechnical and Geoenvironmental Engineering*, *136*(12), 1721–1728. https://doi:10.1061/(ASCE)GT.1943-5606.0000382

Verba, C., Thurber, A. R., Alleau, Y., Koley, D., Colwell, F., & Torres, M. E. (2016). Mineral changes in cement-sandstone matrices induced by biocementation. *International Journal of Greenhouse Gas Control*, *49*, 312–322. https://doi.org/10.1016/j.ijggc.2016.03.019

Warren, L. A., Maurice, P. A., Parmar, N., & Ferris, F. G. (2001). Microbially mediated calcium carbonate precipitation: Implications for interpreting calcite precipitation and for solid-phase capture of inorganic contaminants. *Geomicrobiology Journal*, *18*, 93–115.

Whiffin, V. A., van Paassen, L. A., & Harkes, M. P. (2007). Microbial carbonate precipitation as a soil improvement technique. *Geomicrobiology Journal*, *24*(5), 417–423. https://doi.org/10.1080/01490450701436505

Witherspoon, P. A., Wang, J. S. Y., Iwai, K., & Gale, J. E. (1980). Validity of cubic law for fluid flow in a deformable rock fracture. *Water Resources Research*, *16*(6), 1016–1024. https://doi.org/10.1029/WR016i006p01016

Zhu, T., & Dittrich, M. (2016). Carbonate precipitation through microbial activities in natural environment, and their potential in biotechnology: A review, frontiers in bioengineering and biotechnology. *Frontiers in Bioengineering and Biotechnology*, *4*, 4.